



A new imaging mode based on X-ray CT as prior image and sparsely sampled projections for rapid clinical proton CT

Yu-Qing Yang^{1,2,3,4} · Wen-Cheng Fang^{2,4,5} · Xiao-Xia Huang⁴ · Qiang Du⁶ · Ming Li⁶ · Jian Zheng⁶ · Zhen-Tang Zhao^{2,3,4,5}

Received: 22 March 2023 / Revised: 19 April 2023 / Accepted: 2 May 2023 / Published online: 28 August 2023

© The Author(s), under exclusive licence to China Science Publishing & Media Ltd. (Science Press), Shanghai Institute of Applied Physics, the Chinese Academy of Sciences, Chinese Nuclear Society 2023

Abstract

Proton computed tomography (CT) has a distinct practical significance in clinical applications. It eliminates 3–5% errors caused by the transformation of Hounsfield unit (HU) to relative stopping power (RSP) values when using X-ray CT for positioning and treatment planning systems (TPSs). Following the development of FLASH proton therapy, there are increased requirements for accurate and rapid positioning in TPSs. Thus, a new rapid proton CT imaging mode is proposed based on sparsely sampled projections. The proton beam was boosted to 350 MeV by a compact proton linear accelerator (LINAC). In this study, the comparisons of the proton scattering with the energy of 350 MeV and 230 MeV are conducted based on GEANT4 simulations. As the sparsely sampled information associated with beam acquisitions at 12 angles is not enough for reconstruction, X-ray CT is used as a prior image. The RSP map generated by converting the X-ray CT was constructed based on Monte Carlo simulations. Considering the estimation of the most likely path (MLP), the prior image-constrained compressed sensing (PICCS) algorithm is used to reconstruct images from two different phantoms using sparse proton projections of 350 MeV parallel proton beam. The results show that it is feasible to realize the proton image reconstruction with the rapid proton CT imaging proposed in this paper. It can produce RSP maps with much higher accuracy for TPSs and fast positioning to achieve ultra-fast imaging for real-time image-guided radiotherapy (IGRT) in clinical proton therapy applications.

Keywords Proton CT · Real-time image guidance · Image reconstruction · Proton therapy

1 Introduction

At present, proton therapy is responsible for approximately 85% of hadron therapy cases in daily tumor treatments conducted at a very high speed [1]. Owing to its Bragg peak characteristics, most of the energy will be released at the lesion, thus reducing the loss of healthy human tissues and

This work was supported by the Research collaboration on Thailand's new synchrotron light source facility (SPS-II) (No. ANSO-CR-KP-2020-16).

✉ Wen-Cheng Fang
fangwencheng@zjlab.org.cn

✉ Qiang Du
duq@sibet.ac.cn

¹ Shanghai Institute of Applied Physics, Chinese Academy of Sciences, Shanghai 201800, China

² University of Chinese Academy of Sciences, Beijing 100049, China

³ School of Physical Science and Technology, ShanghaiTech University, Shanghai 201210, China

⁴ Shanghai Synchrotron Radiation Facility, Shanghai Advanced Research Institute, Chinese Academy of Sciences, Shanghai 201204, China

⁵ Shanghai Key Laboratory of Cryogenics and Superconducting RF Technology, Shanghai, China

⁶ Suzhou Institute of Biomedical Engineering and Technology Chinese Academy of Sciences, Suzhou, China

cells. However, both proton and photon therapies use X-ray CT for TPSs. The HU values are then transformed to an RSP map. This process has an intrinsic error in the range of 3–5% [2]. It can lead to serious effects on sensitive organs and blood vessels. Proton CT is able to address this error and reduce the error associated with organ movement when the patient is transferred to the treatment room. FLASH also has become a new focus in tumor radiotherapy owing to its ultra-high dose rate (FLASH > 35 Gy/s) properties [3]. Therefore, more stringent requirements for more precise localization of tumor lesions and better IGRT have been introduced. The first domestic proton therapy device has entered the clinical stage at the Ruijin Hospital Proton Therapy Center, Shanghai Jiaotong University School of Medicine. The proton CT imaging project is expected to be housed in the fifth treatment room for experimental validations and presents a more realistic requirement for rapid proton CT imaging of clinical significance.

Proton CT has research teams around the world, but it is only in the experimental stage at present. It has not been used in clinical practice owing to various limitations. For example, in experiments, phantoms are rotated to obtain projection information from different angles; however, this scheme is not applicable to patients clinically [4–8]. While in clinical proton therapy, the use of omnidirectional irradiation at 180 angles may not be feasible for proton CT owing to the long duration required for rotation. Therefore, the identification of ways to achieve rapid proton imaging to obtain accurate RSP maps for TPSs in clinical practice has become the focus of attention. Moreover, traditional gantry types use heavy magnets. If proton CT is integrated into the gantry and rotates with it, it will take a long time for proton irradiation owing to the time required for rotation. To realize accurate RSP reconstruction in a very short time, it is a good consideration to combine proton CT with X-ray CT. Thus, reducing the number of irradiation angles is the most direct and efficient way to achieve rapid proton imaging. Meanwhile, a design of superconducting gantry different from conventional therapy gantry has been proposed [9] that is also capable of increasing the speed of the proton irradiation process. The energy range of existing proton therapy is 70–235 MeV, but this is insufficient for proton imaging [10]. Compared with proton irradiation at 230 MeV, the scattering at 350 MeV is less extensive and the proton beam would deposit smaller doses in the human body.

In this study, a new proton CT imaging mode is presented from sparsely sampled projections based on X-ray CT as the prior image for rapid clinical proton CT. The proton beam is boosted to 350 MeV by a compact proton LINAC. The high-energy proton beam keeps the Bragg peak completely out of human body, and it has a major dose advantage compared with X-ray CT. The feasibility of the enhancement of the proton energy from 230 to 350 MeV is also verified [11].

Furthermore, a similar structure used to accelerate protons is cold-tested and the result shows that the design is feasible [12, 13]. To achieve sparse angle proton imaging, the X-ray CT image is used as the prior image. The X-ray CT is transformed into the RSP map by HU-RSP transformation curve for initial iterations, and then the image reconstruction will be conducted by using 12 parallel proton beam irradiation. The X-ray CT can be any one the patient had before proton therapy, while it must be consistent with the proton CT so as to provide sufficient accurate prior information. Here are the reasons for choosing 12 angles for imaging. A static superconducting therapy gantry based on 12 superconducting coils is proposed for proton therapy [9]. The position of the coils is the irradiation direction of the proton beam. Proton therapy can be realized rapidly based on ultra-fast beam allocation and ultra-fast proton scanning technology using an advanced deflector with variable polarization. It is known that fast scanning systems take approximately 10 μ s to scan an energy layer [9], and the acquisition process of one angle could be finished within 1 ms. Thus, 12-angle proton projections would be finished within 12 ms. The rapid completion of proton CT image reconstruction with X-ray CT prior image can be achieved through hardware, combined with efficient proton detection technology. The entire implementation of proton CT is planned to be completed within several hundred milliseconds. After proton imaging, the gantry could quickly transform energy to perform proton therapy. The static superconducting gantry is programmed to perform proton FLASH therapy within 100 ms [9], so the proton CT and subsequent proton FLASH therapy would take a total of 1 s [11]. By this way, it can not only improve the speed of proton CT, but also reduce the errors of TPS caused by organ movement. It is of great clinical significance to realize IGRT in proton treatments in the future.

2 Methods

The energy of the proton beam can be enhanced to 350 MeV by the S-band high-gradient acceleration structure. The information of the proton passing through the object can be tracked and recorded so that reconstructed algorithms can be used for proton imaging. This section introduces the principle and reconstruction algorithm for this imaging mode.

2.1 Principle of the 350 MeV proton CT imaging mode based on X-ray CT as prior image

In this study, the proton beam was boosted from 230 to 350 MeV. Because the sparse scanning at 12 angular projections is not enough for accurate proton image reconstruction, an X-ray CT image is used as a prior image. To use an X-ray CT image for reconstruction, the transformation relationship

between HU and RSP is usually determined experimentally using the devices available in the clinic. Different phantoms of multiple known materials are irradiated with X-ray and protons respectively, and the data are interpolated and fitted according to the HU value and RSP to obtain the transformation relationship [14, 15]. Therefore, the transformed HU to RSP (HU–RSP) map can be obtained for rapid proton image reconstruction to obtain a more accurate RSP map for TPSs. In this paper, GEANT4 simulation was used for verification, so X-ray CT and proton CT were simulated respectively. The specific process is shown in Fig. 1.

The proton CT system mainly consists of two parts, as shown in Fig. 2a. The proton beam enters from the left side. The tracking detectors are used to record the transverse position in the upstream and downstream directions with respect to the patient, and a residual range detector is used to determine the proton energy loss in the process. Thus, the water-equivalent path length (WEPL) of the proton can be calculated as it passes through the patient using a calibration procedure [16]. The WEPL value of the proton is defined as the integral of the material's RSP along the proton path L through the object. The RSP is defined as the ratio of the stopping power (SP) of the specific material of the object to the SP of water [17]. It is assumed that the energy of an incoming proton is equal to that of a proton ejected from the accelerator. The information is collected as the basis to reconstruct the RSP map [18].

The energy of proton beam can be increased from 230 to 350 MeV based on S-band high-gradient accelerating technology. The S-band high-gradient acceleration structure meets the requirements of small and compact facilities and can be used in single-treatment rooms and for FLASH proton therapy [11]. The proton beam is accelerated and can be transmitted directly into the treatment room for proton imaging and proton therapy. This method has been simulated and proved to have sufficient capture rate [11]. To increase the beam's energy using the LINAC, cold-state technology made the linear acceleration section shorter; this also requires more complex control technology [19–21]. The superiority of the 350 MeV proton beam was verified using different proton beams which passed through different phantoms. The proton pencil beams at 230 MeV and 350 MeV were used. Furthermore, the phantoms used in simulations were (a) a cube of water with a length of 15 cm and (b) a

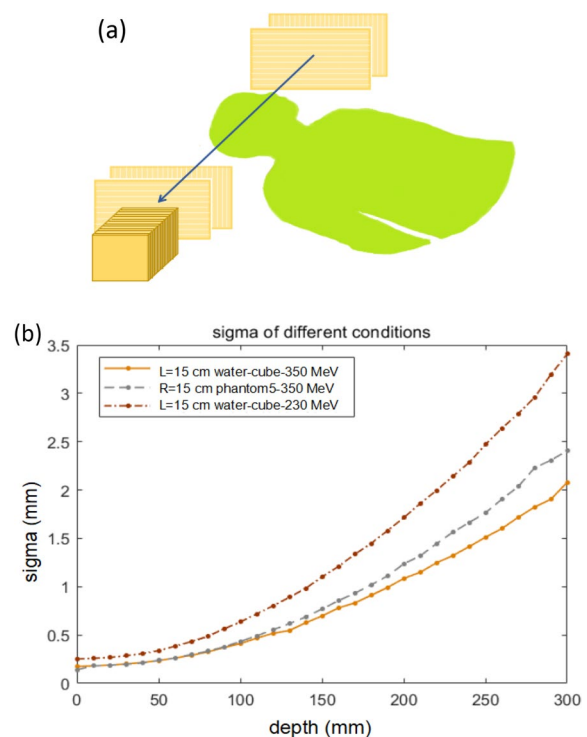
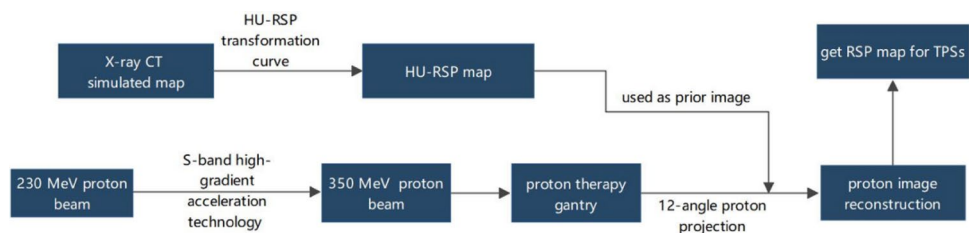


Fig. 2 (Color online) **a** Illustration of the proton CT system. **b** Comparison of sigma values between 230 and 350 MeV proton pencil beam passing through different phantoms. Phantom 5 represents the sphere with a radius of 15 cm. The materials used are water, Teflon, air, polyvinyl chloride (PVC), and bone

sphere with a radius of 15 cm which comprised five different materials. The sigma values were recorded every 10 mm. Sigma is the standard deviation from the Gaussian fit of the proton beam. As shown in Fig. 2b, the sigma values of the 350 MeV proton beam were smaller than those of the 230 MeV in both phantoms, that is, the scattering of the 350 MeV proton beam was less extensive. When 350 MeV protons pass through the phantom constructed with multiple materials, they scatter more than the cases in which they pass through the cube of water. For sensitive human organs, proton CT of high energy can play a better protective role. Additionally, the equivalent water depth of the 350 MeV proton beam is approximately 653 mm to ensure that the Bragg peak falls outside of the human body to reduce the dose. Finally, the dose of proton CT was approximately

Fig. 1 Overview of the rapid proton CT imaging mode with an X-ray CT image used as prior image



30 mGy in simulations, which was lower than that of X-ray CT. Thus, the importance of the 350 MeV proton beam for proton imaging is evident.

2.2 Proton image reconstruction algorithms

Similar to X-ray CT, proton image reconstruction algorithms can be divided into two categories: filtered back projection (FBP) and iterative. However, FBP requires enough sampling angles. To achieve fast proton CT imaging in this study, iterative reconstruction was considered to achieve high-quality image. Three iteration methods were considered, namely, the algebraic reconstruction technique (ART), compressed sensing (CS) image reconstruction, and prior image-constrained compressed sensing (PICCS) image reconstruction. The basic principle is to select an initial matrix for iteration until the final criterion is met. The criterion can choose a standard value or stop after reaching the set number of iterations. The differences pertain to the iterative equations of the three methods.

ART is one of the simplest methods used to reconstruct images from measured projections. The RSP value is represented by x . The consistency condition should be satisfied [22, 23],

$$\mathbf{A}x = \mathbf{b}. \quad (1)$$

Iterative reconstruction is consistent in the least-squares method. In proton CT applications, vector \mathbf{b} describes the measured WEPL value, and \mathbf{A} represents the system matrix. The system matrix \mathbf{A} is an $M \times N$ matrix whose elements represent the contribution of the i th projection to the j th pixel. Commonly, a_{ij} can represent the length of intersection between the proton path i th and pixel j th, or the intersection probability of each mesh j th and path i th. The calculation of projection matrix \mathbf{A} directly affects the reconstruction speed of the entire algorithm.

The sparse image will be reconstructed iteratively by minimizing the ℓ_1 norm. The ℓ_1 norm is defined as the summation of the absolute value of all function values. Additionally, the conditions of Eq. (1) should also be satisfied. In PICCS, the sparseness of the target image is a prior image in the algorithm. That is, the image can be sparsified by the subtraction operation, where $F - F_p$. F_p represents the prior image. The sparsifying transforms, which include the discrete gradient transform and wavelet transforms, would be utilized to sparsify the subtracted image after the subtraction. In this study, the total variation term, $TV(F)$, was used. It was defined as the ℓ_1 norm of the discrete gradient of the image. The parameter α ($0 \leq \alpha \leq 1$) was selected based on the degree of similarity between the prior image F_p and the reconstructed image F . When α was set to zero, the PICCS algorithm was reduced to the CS algorithm [24, 25].

To compare the reconstruction results of various algorithms mentioned above, the reconstructed image was quantitatively compared with the actual phantom image. In this study, the normalized mean square distance d and the normalized mean absolute distance criterion r were calculated for each algorithm. The definitions of these two parameters are listed below [26, 27]. Furthermore, the accuracy of RSP was expressed as $Diff$.

$$d = \left[\frac{\sum_{u=1}^N \sum_{v=1}^N (t_{u,v} - r_{u,v})^2}{\sum_{u=1}^N \sum_{v=1}^N (t_{u,v} - t_{\text{mean}})^2} \right]^{1/2} \quad (2)$$

$$r = \frac{\sum_{u=1}^N \sum_{v=1}^N |t_{u,v} - r_{u,v}|}{\sum_{u=1}^N \sum_{v=1}^N |t_{u,v}|} \quad (3)$$

$$Diff = \frac{RSP_{\text{real}} - RSP_{\text{rec}}}{RSP_{\text{real}}} \times 100\% \quad (4)$$

where $t_{u,v}$ and $r_{u,v}$ represent the pixel RSP value of row u and column v in the original and reconstructed images of the phantom, respectively, and t_{mean} is the average pixel value of the object. The image has $N \times N$ pixels. The smaller the d value is, the better the quality of the image. Additionally, RSP_{real} represents the real RSP value, and RSP_{rec} represents the RSP of the reconstructed image.

3 Results

In this study, proton CT and X-ray CT platforms were constructed based on Monte Carlo simulations. The software platform for proton CT simulations consisted of GEANT4 [28] simulations, WEPL calibration, and image reconstruction. For GEANT4 simulations, specific models and parameters needed to be determined in three dimensions, such as the detector parameters, the properties of the proton beam, phantom, and the physical process. One of the important steps in proton CT was the determination of the energy lost when the proton traveled a fixed distance within the object [29]. After data fitting, the two-dimensional projection data of protons can be obtained using the quadratic relationship. Similarly, it is necessary to set detector parameters and the X-ray energy to reconstruct the X-ray image according to the attenuation of the X-ray passing through the object. The proton projection data (acquired at 12 angles) and the HU-RSP map were used for image reconstruction.

3.1 Most likely path estimated to identify accurate proton position

To reconstruct the proton image, based on an appropriate multiple Coulomb scattering theory, a likely proton path

within the phantom can be calculated if the entry and exit positions are given. The position and angle detector system is able to measure the position and direction of each proton accurately. Thus, it is possible to estimate the proton paths through the object using the information. Proton path estimation can be divided into three types: straight line path (SLP), cubic spline path (CSP), and MLP. A SLP is the simplest estimation, which is defined by the line between the position in and out of the object. Because the positions and tangential directions of each proton at the entrance and exit are known, the two endpoints can be fitted with smooth curves to obtain the estimated CSP; these are mathematically simpler than that of the MLP. However, it is considered that the MLP is the best statistical estimate of the path curve when a proton passes through a homogeneous medium. The paths estimated are supposed to be incorporated into an iterative reconstruction algorithm.

The internal paths follow a certain probability distribution. The MLP can be defined as the maximum likelihood problem of Bayesian statistics [30, 31]. The position and direction of an incoming proton are set to be A (0, 0, 0), and the exit position and direction are set to be B (u_1, t_1, θ_1). The MLP y_{mlp} in a uniform object can be obtained by the following Eq. 5

$$y_{mlp} = \left(\sum_1^{-1} + R_1^T \sum_2^{-1} R_1 \right)^{-1} \left(\sum_1^{-1} R_0 y_0 + R_1^T \sum_2^{-1} y_2 \right). \quad (5)$$

Every term of the equation listed above has a detailed calculation method [31]. To calculate the elements of the scattering matrices, the proton speed relative to the velocity of light and proton momentum at different depths, $1/\beta^2 p^2$, could be derived using GEANT4 simulations. In the simulations, the 350 MeV protons traversed a uniform cubic phantom of water with a length of 200 mm. It was approximated by a fifth-degree polynomial. The fitted coefficients are shown in Table 1. As shown in Fig. 3, the information of two protons was randomly recorded from a simulation, and the CSP, MLP, and the associated error envelopes were calculated. Note that the proton entered from the right. The figure shows that the MLP and CSP are closer to the real path compared with the SLP. By calculating the root-mean-square error (RMSE) in the central region, the SLP, CSP, and MLP were 0.764 mm, 0.443 mm, and 0.422 mm, respectively. The RMSE of the SLP was approximately two times higher than that of the MLP, while the RMSE of the MLP was slightly smaller than that of the CSP. It could be proved that MLP is more accurate for proton path estimations.

3.2 Optimization of algorithms to improve the performance of reconstruction image

Through the continuous improvement of image reconstruction, the imaging mode using the HU-RSP map as the prior image for proton imaging was preliminarily verified using the reconstructed algorithms listed above. A spherical water phantom with a diameter of 25 cm was built with two small balls of different materials and different sizes inside. Projection data were collected in GEANT4 by irradiation using a

Table 1 GEANT4 simulation results of the fitted polynomial to the average value of $1/\beta^2 p^2$ as a function of depth when a proton parallel beam passes through a water cube (depth of 200 mm)

Coefficients	Values
a0	2.737×10^{-6}
a1	4.458×10^{-8}
a2	7.738×10^{-10}
a3	-2.126×10^{-12}
a4	9.772×10^{-13}
a5	-1.403×10^{-14}

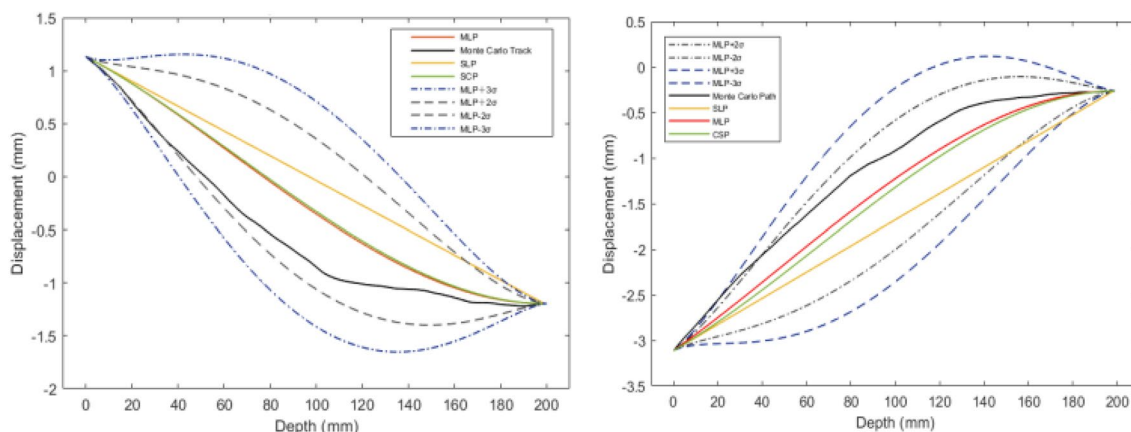


Fig. 3 (Color online) Examples of two proton tracks in simulation. The tracks of the straight line path (SLP), cubic spline path (CSP), and the most likely path (MLP) with associated 2-sigma and 3-sigma error envelopes are shown. The two histories lie within the error envelopes

350 MeV parallel proton beam at 12 angles. For verification, the whole values of the standard image were uniformly increased; this was then used as a prior image to represent the image converted to RSP from X-ray CT. Figure 4a, b, and c are the image reconstruction results using ART, CS, and PICCS, respectively. Visually, there are obvious artifacts in the image reconstructed by ART in Fig. 4a. In contrast, the image quality of the reconstructed image using PICCS was improved considerably without artifacts in the biggest circle in Fig. 4c. At the same time, the values of d and r of the three algorithms were also calculated. These values are plotted as a function of the iteration number, as shown in Fig. 4d. From a longitudinal perspective, the values decrease as a function of the number of iterations, that is, the reconstruction effect improves. However, eventually, it will reach a steady state. Horizontally, the values of d and r of PICCS are lower, and the image quality improves considerably. After 100 iterations, the corresponding d values of ART, CS and PICCS are 0.174, 0.147, and 0.131, and the corresponding r values are 0.1, 0.098 and 0.086, respectively. When the picture was

rotated 45° clockwise, the RSP values of line 262 was used for comparison, as shown in Fig. 4e. The yellow solid line represents the real RSP values, and the yellow dashed line represents the values of prior image. The ART reconstructed result has more noise, and the CS reconstructed result is poor in the edge of the material. While the PICCS reconstructed result is in good agreement with the initial value. In PICCS algorithm, the choice of α is very important [32, 33]. It depends on the quality of prior images. Because the RSP deviation of each pixel is uniform distributed in this prior image and accurate information is also provided at the boundary, α is chosen as 0.95 after tuning the parameters. When the quality of prior image is poor, α would take a smaller value. The RSP distribution image obtained through HU-RSP transformation can provide relatively accurate prior information at present, thus the introduction of this prior information is very necessary, which determines that the value of α cannot be too small. However, the specific value of α needs to be determined after tuning according to different experimental conditions. According to the calculation

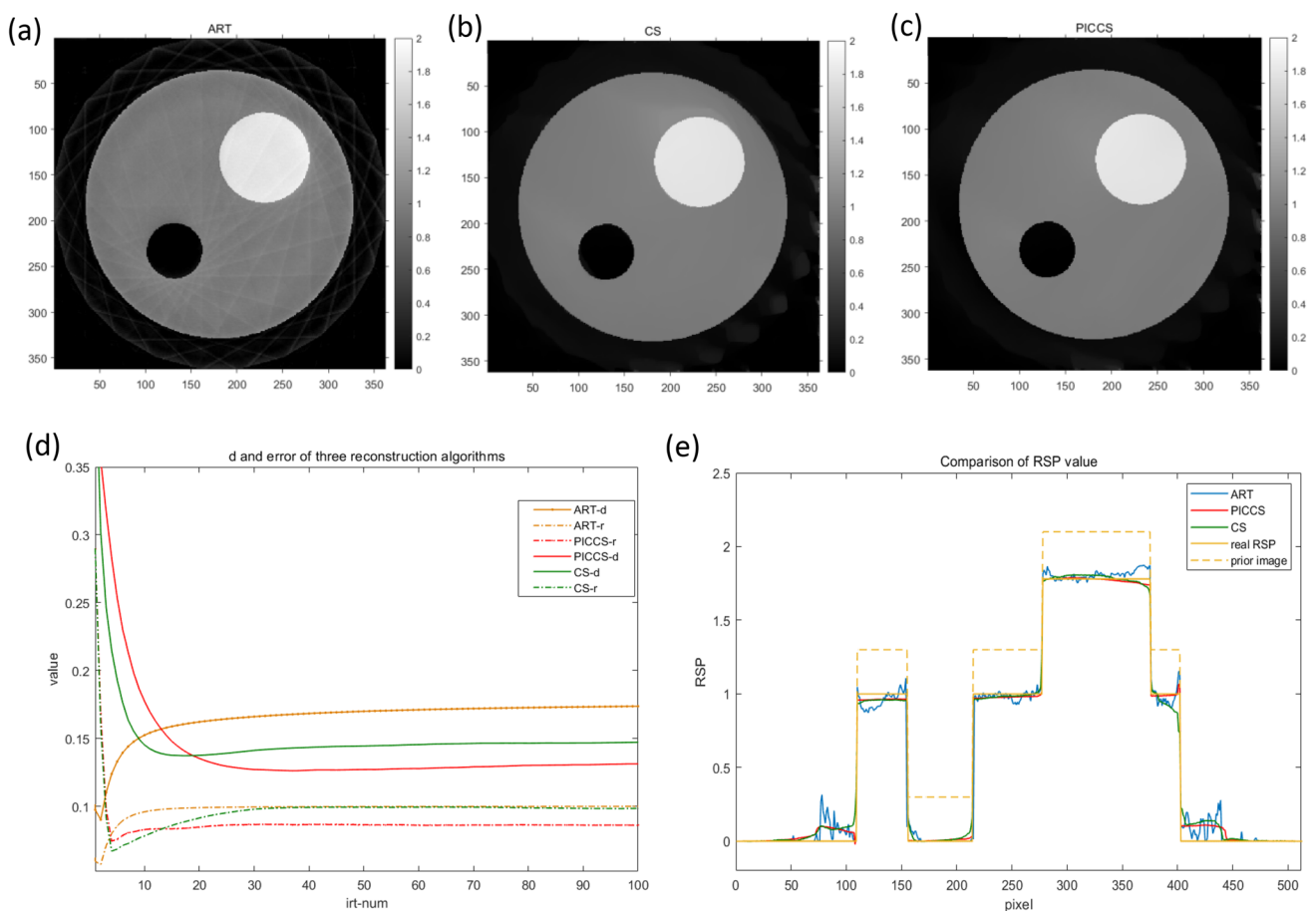


Fig. 4 **a** Image reconstructed with ART. **b** Image reconstructed with CS. **c** Image reconstructed with PICCS. **d** Plots of d and r values as a function of iteration. **e** Comparison of the profiles of the three algo-

gorithms. The yellow, blue, green, and red solid lines respectively represent the real RSP value, ART result, CS result and PICCS result. The yellow dashed line represents the RSP value of prior image

results of d and r , PICCS yields a better outcome when the proposed method is used in conjunction with a prior image with proton irradiation at 12 angles. Therefore, Monte Carlo simulations would be used to obtain X-ray and proton CT images of different phantoms to verify the imaging mode proposed in this paper.

There are many factors affecting the reconstruction of proton CT image, which will affect the accuracy of the final reconstruction of RSP. Currently, semiconductor detectors can achieve resolution up to the micron level, which is sufficient for proton CT. Thus in this paper, the energy resolution of residual energy detector and the angle accuracy of proton CT integrated gantry were analyzed. In GEANT4, 350 MeV parallel proton beam was used to collect 12 angle projection information of Phantom2. And the PICCS algorithm was used for reconstruction. Firstly, the allowable error range of the residual energy detector is analyzed. The deviation between the proton energy used for image reconstruction and the real residual energy detected was set as $0, \pm 0.5, \pm 1$ and ± 2 , respectively. The values of d and r of the reconstructed images under different circumstances were calculated respectively. The calculated results are shown in Table 2. By comparing the d and r results, it can be inferred that the accuracy of the reconstructed RSP values are close to the real values with the cases of ± 0.5 and ± 1 . In other words, the energy resolution in the range of 0.3–0.6% can realize the error tolerance of the image reconstruction. Secondly, the range of the allowed error of the gantry angle was verified in GEANT4 simulation. The deviations between the projection angle in the reconstruction algorithm and the actual irradiation angle in the simulation were set as $0^\circ, +0.2^\circ, +0.5^\circ$ and $+1^\circ$, respectively, so as to assume the angle accuracy deviation of the therapy gantry. This is because we realized proton projection information acquisition from different angles by rotating phantom in the simulation. The 0° deviation represents the standard case. The quantitative calculation results are shown in Table 3. By comparison, it is found that when the deviations are 0.5° and 1° , the values of d and r are larger than that of the standard case. Therefore, when the angle deviation of the gantry is within 0.2° , the reconstruction result is within the allowable error range. Moreover, the angle accuracy of the therapy gantry of the first domestic proton therapy demonstration device is within 0.2° , which provides favorable

Table 2 The d and r values of reconstructed images with different energy resolutions

Δ_E	0	± 0.5	± 1	± 2
d	0.073	0.072	0.073	0.08
r	0.025	0.025	0.026	0.029

Table 3 The d and r values of reconstructed images with different angle accuracy of the therapy gantry

Δ_{theta}	1°	0.5°	0.2°	0°
d	0.146	0.086	0.075	0.073
r	0.076	0.027	0.027	0.025

experimental conditions for the subsequent proton CT experiments.

3.3 Rapid proton CT imaging based on X-ray CT image used as the prior image

X-ray CT images produced by Monte Carlo simulations were used in this section. In the Monte Carlo simulations of X-ray CT, the goal was to generate simulated CT images. Projection data with relative errors $\leq 0.75\%$ were collected at 180 angles in half a circle using a 60 keV parallel photon beam and were reconstructed based on the traditional FBP algorithm. The detector layer was constructed with 400 pixels with a 1 mm width. By comparison, PICCS reconstruction results were better when the same conditions were used. Furthermore, two phantoms were selected for the simulations. Figure 5a shows the phantom composed of four different materials. The largest sphere was made of water (radius = 12.5 cm). Inside it, there were three different spheres made of different materials (radii = 2, 1.5, 1, and 0.5 cm). The materials used for each group were Teflon, PMMA, and air. Figure 5b shows the other phantom composed of five different materials, and the densities of the materials were closer to the soft tissue of the human body. The materials inset were POM, PMP, PMMA, and Epoxy [14]. All the diameters were equal to 1.5 cm, and the radius of the largest sphere was 10 cm. The two phantoms of Fig. 5 are referred to Phantom2 and Phantom3 in this article.

To verify the feasibility of rapid proton CT imaging mode proposed in this paper, the PICCS method was used to verify the proton image reconstruction using 180, 120, 60, 30 and 12 proton projection angles, as well as the FBP method with

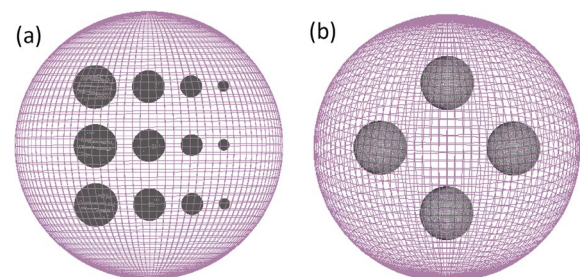


Fig. 5 (Color online) Diagrams of the two phantoms used in GEANT4 Monte Carlo simulations

180 angles. The initial iteration matrix of the reconstruction was a zero matrix. The RSP values of the corresponding materials in the same area and their errors were also calculated. The specific results are listed in Table 4. It can be seen that the value of $Diff$ increases significantly when the number of projection angles is 30 and 12. Especially, when the projection angle number is 12, the reconstruction error is maximum. Though the $Diff$ of Teflon and PMMA do not follow a clear trend, this simulation is aimed to serve as a reference and comparison for the imaging mode proposed in this paper. It is to demonstrate that the proposed imaging mode based on prior image with 12 sparse angles can achieve the same magnitude of reconstruction results as when the number of projection angles is larger. Meanwhile, it is considered that the results of 180 and 120 are basically in the range of standard values. Due to the influence of systematic error of the simulated proton CT, the value of reconstructed RSP may fluctuate. It is within the error of the system. The multi-angle proton CT imaging mode can achieve relatively accurate image reconstruction, but the speed was not adequately high owing to the larger number of proton scanning angles.

The numbers of angles in PICCS were 180, 120, and 60, and the initial iteration matrix was a zero matrix. RSP_{ref} represents the RSP value for reference, $RSP_{P_{180}}$ represents the reconstructed RSP value of the PICCS method with 180 angles. $Diff_{P_{180}}$ represents the error of PICCS method with 180 angles. $RSP_{P_{120}}$ and $Diff_{P_{120}}$ represent the two indexes of the PICCS method of 120 angles. $RSP_{P_{60}}$ and $Diff_{P_{60}}$ represent the two indexes of the PICCS method of 60 angles. RSP_{FBP} and $Diff_{FBP}$ represent the two indexes of the FBP method of 180 angles.

The HU-RSP images of the two phantoms are shown in Fig. 6a, c. In the case of Phantom2, the transformed RSP values of Teflon, PMMA, and water were 1.467, 1.081, and 0.972, respectively. The percentage difference between them and the standard RSP values were 18.04%, 6.81%, and 2.8%, respectively. Comparisons showed that the errors of RSP obtained from materials with higher density were larger; this outcome is similar to the experimental conclusions [34]. Proton reconstruction was performed using 12 angular

proton projections within 180° . In the reconstruction process, it was found that the deviation from the real RSP value of materials with different densities were different. Thus, the same algorithmic parameters may not make all the materials reach the closest RSP values at the end of the iterations. In the PICCS algorithm, if the increment factor is too large, the correction will be too large, and the correlation between the reconstructed image and the projected data would become worse. Therefore, different PICCS parameters were set in image reconstruction according to the densities of the different materials. For material media such as densified bone with large conversion error, the number of TVM setting in PICCS is less. In addition, because the RSP distributions of prior images are uneven and has obvious noise, α is set as 0.2 after tuning the algorithm parameters. The reconstruction results are shown in Fig. 6b, d. The reconstruction results in Tables 5 and 6 are the results of Phantom2 and Phantom3, respectively. RSP_{prior} represents the RSP of the HU-RSP map. Moreover, RSP_{PICCS} represents the reconstructed value with the PICCS method. $Diff_{prior}$ represents the error percentage between the value of HU-RSP map and the true value. $Diff_{PICCS}$ represents the error percentage between the reconstructed and the true values.

According to the reconstruction results, the average RSP values of all the materials were calculated. Firstly, the reconstruction results of Phantom2 were analyzed. By setting PICCS parameters, the reconstructed RSP values of Teflon, PMMA, and water were 1.769, 1.13, and 1.01, respectively. Compared with the prior image, the reconstructed RSP values of PICCS were more accurate. The errors between reconstructed and actual values were 1.17%, 2.59%, and 1%. Figure 6b shows a clear image with good quality. This verifies that the imaging mode proposed in this study is feasible, and the PICCS algorithm can also yield relatively accurate RSP results. As the RSP deviation of Teflon in Phantom2 was larger than others, the algorithm was applied to Phantom3 to verify the feasibility of the imaging mode. The densities of materials in Phantom3 were all close to that of soft tissues in the human body. The constructed RSP values of POM, PMP, PMMA, and Epoxy were 1.340, 0.865, 1.13,

Table 4 Reconstructed results of PICCS and FBP of Phantom2

Material	RSP_{ref}	$RSP_{P_{180}}$	$Diff_{P_{180}}$ (%)	$RSP_{P_{120}}$	$Diff_{P_{120}}$ (%)	$RSP_{P_{60}}$	$Diff_{P_{60}}$ (%)
Teflon	1.79	1.818	1.56	1.809	1.06	1.81	1.12
PMMA	1.16	1.14	1.72	1.144	1.38	1.139	2.67
Water	1.00	1.01	1.0	0.980	2.0	0.981	1.9
Material	RSP_{ref}	$RSP_{P_{30}}$	$Diff_{P_{30}}$ (%)	$RSP_{P_{12}}$	$Diff_{P_{12}}$ (%)	RSP_{FBP}	$Diff_{FBP}$ (%)
Teflon	1.79	1.75	2.23	1.733	3.18	1.80	0.56
PMMA	1.16	1.06	8.6	1.054	9.14	1.126	2.93
Water	1.00	0.98	2.0	0.90	10.0	0.95	5.0

Fig. 6 Reconstructed results of two phantoms with the PICCS method. **a** HU–RSP map of Phantom2. **b** Reconstructed map of Phantom2 using 12 angular projections. **c** HU–RSP map of Phantom3. **d** Reconstructed map of Phantom3 using 12 angular projections

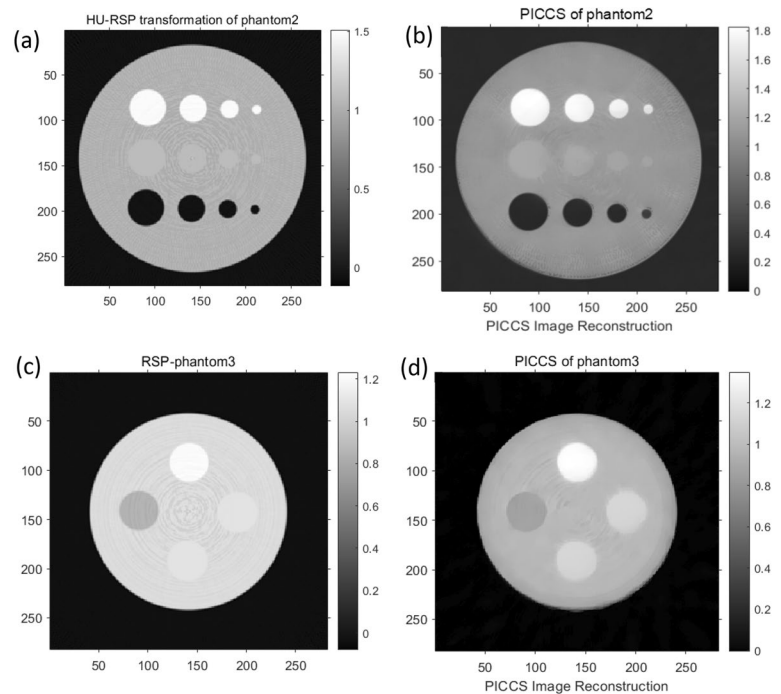


Table 5 Comparisons of reconstructed RSP values with the value of the HU–RSP map of Phantom2

Material	RSP_{ref}	RSP_{prior}	$Diff_{prior} (%)$	RSP_{PICCS}	$Diff_{PICCS} (%)$
Teflon	1.79	1.467	18.04	1.769	1.17
PMMA	1.16	1.081	6.81	1.13	2.59
Water	1.00	0.972	2.8	1.01	1.0

Table 6 Comparisons of reconstructed RSP values with the value of HU–RSP map of Phantom3

Material	RSP_{ref}	RSP_{prior}	$Diff_{prior} (%)$	RSP_{PICCS}	$Diff_{PICCS} (%)$
POM	1.359	1.204	11.33	1.340	1.40
PMMA	1.16	1.088	6.21	1.13	2.58
EPOXY	1.144	1.089	4.72	1.127	1.49
PMP	0.88	0.844	4.09	0.865	1.70

and 1.127, respectively. In addition, the RSP values of prior images of Phantom3 were 1.204, 0.844, 1.088, and 1.089, respectively. All the reconstructed RSP values were closer to the actual RSP values. The percentage differences between them and the standard RSP were decreased. For instance, the error of POM decreased from 11.33% to 1.40%, and the error of PMP decreased from 4.09% to 1.7%. However, the impact of noise generated in X-ray CT was smaller compared with the error in the transformation of HU to RSP. The two RSP values of the materials in the simulation, namely RSP_{prior} and RSP_{PICCS} , were fitted as shown in Fig. 7. The

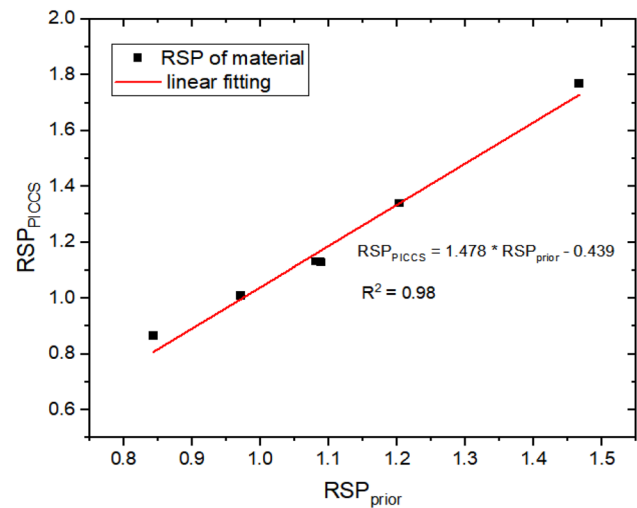


Fig. 7 Fitting regression and scatter plot of RSP_{prior} and RSP_{PICCS}

correlation coefficient R^2 was 0.98. These findings showed that the transformation of HU–RSP yielded different deviations in different materials and indicated that the fractional RSP algorithm was effective for proton reconstruction using X-ray CT as the prior image. It should be noted that the reconstruction error of PMMA using proton imaging at 60 angles was also approximately equal to 1.14. This error may be attributed to the Monte Carlo simulation.

By comparing the results of the 12-projection imaging mode using the HU–RSP map as the initial iteration with the results of multi-angle proton imaging in this chapter, it was

found that this mode could achieve the same expectations and yield similar results to those obtained by proton imaging. For example, for POM, the RSP error of the reconstructed image was reduced from 11.33% to 1.4%. For Teflon, the simulation error of the imaging mode proposed was 1.17%, and in the case that the number of scanning angles was 180, 120, 60 in PICCS, the errors were 1.56%, 1.06%, and 1.17%, respectively. The reconstruction results from only 12 angles can achieve similar results with those from more angles.

In the simulation, the data acquisition speed associated with 12 angular projections was higher than that for sixty or more angular projections and it took less time to complete the 12-angle image reconstruction algorithm; this ensured that the speed of the whole proton imaging would be improved, including proton scanning and proton image reconstruction. Therefore, in this process, the displacement of organs caused by breath movement can also be weakened to a certain extent. The simulation experiments in this paper verify that this imaging mode proposed can reduce the prior image conversion error, and the reconstructed RSP error is about 2%. It could be verified that rapid proton CT imaging mode is feasible using only 12 angular projections and the X-ray CT image as the prior image. However, the prior image in the simulation was not processed with artifacts. The value of α in PICCS is set to 0.2, also in order to reduce the influence of noise in prior images. However, it is inevitable to introduce the noise in the prior image. Clinical photon CT has matured; thus, clinical X-ray CT proton imaging can yield images with much higher image quality. This indicates that the proton CT imaging mode proposed would still improve the accuracy of RSP even if the prior image quality is poor, let alone if the prior image quality is good. At the same time, it also reduces the requirement for the error range of RSP distribution images obtained through HU-RSP transformation in clinic. In the future, the algorithm needs to be improved to improve the RSP accuracy. Therefore, the reconstructed RSP error is expected to be much smaller. For example, owing to multiple Coulomb scattering, protons would be scattered when they pass through the object boundaries of different materials. The accurate reconstruction of the edge is of vital importance. Besides, due to the static superconducting therapy gantry can deflect the proton beam at different angles through the deflection cavity, proton scanning can be achieved quickly. 3D proton CT image reconstruction and further conditions for the clinical application of the proton CT imaging mode proposed in this paper would be studied.

4 Conclusion

This paper proposed and implemented a new proton CT imaging mode based on the 350 MeV proton beam using 12 angular projections to achieve rapid proton image reconstruction. This imaging mode combined proton and X-ray

CT using the RSP map obtained from the conversion of the X-ray CT acquired as the prior image for TPSs. The MLP was estimated. Furthermore, the PICCS algorithm yielded better results for this imaging mode. X-ray and proton CT images were simulated using Monte Carlo simulations. Comparisons using the map obtained from the HU-RSP transformation showed that the imaging mode can improve effectively the range accuracy. A project was approved to construct a proton CT prototype to verify the principles and the imaging outcomes described herein. It is beneficial to realize a leapfrog development pertaining to proton CT from the experimental to the clinical stages.

Author contributions All authors contributed to the study conception and design. Material preparation, data collection and analysis were performed by Yu-Qing Yang, Wen-Cheng Fang and Qiang Du. The first draft of the manuscript was written by Yu-Qing Yang and all authors commented on previous versions of the manuscript. All authors read and approved the final manuscript.

Data availability The data that support the findings of this study are openly available in Science Data Bank at <https://www.doi.org/10.57760/sciencedb.09386> and <https://cstr.cn/31253.11.sciencedb.09386>.

Declarations

Conflict of interest Wen-Cheng Fang and Zhen-Tang Zhao are editorial board members for Nuclear Science and Techniques and was not involved in the editorial review, or the decision to publish this article. All authors declare that there are no competing interests.

References

1. Particle Therapy Cooperative Group (PTCOG) Collaboration. <https://www.ptcog.com>.
2. M. Yang, X.R. Zhu, P.C. Park et al., Comprehensive analysis of proton range uncertainties related to patient stopping-power-ratio estimation using the stoichiometric calibration. *Phys. Med. Biol.* **57**(13), 4095–4115 (2012). <https://doi.org/10.1088/0031-9155/57/13/4095>
3. E.S. Diffenderfer, B.S. Srensen, A. Mazal et al., The current status of preclinical proton FLASH radiation and future directions. *Med. Phys.* **49**(3), 2039–2054 (2022). <https://doi.org/10.1002/mp.15276>
4. F. Ulrich-Pur, T. Bergauer, A. Burkner et al., Demonstrator for a proton CT system at MedAustron. arXiv: Instrumentation and detectors. 2020. <https://doi.org/10.48550/arXiv.2003.00115>
5. M. Esposito, C. Waltham, J.T. Taylor et al., PRaVDA: the first solid-state system for proton computed tomography. *Phys. Med.* **55**, 149–154 (2018). <https://doi.org/10.1016/j.ejmp.2018.10.020>
6. G. Dedes, H. Drosten, S. Gtz et al., Comparative accuracy and resolution assessment of two prototype proton computed tomography scanners. *Med. Phys.* **49**(7), 4671–4681 (2022). <https://doi.org/10.1002/mp.15657>
7. R.P. Johnson, V.A. Bashkurov, G. Coutrakon et al., Results from a prototype proton-CT head scanner. *Phys. Procedia.* **90**, 209–214 (2017). <https://doi.org/10.1016/j.phpro.2017.09.060>
8. S. Beddar, C.D. Darne, D.G. Robertson, Development of a novel proton CT system using a 3D scintillator detector. *J. Phys. Conf. Ser.* **2167**(1), 012021 (2022). <https://doi.org/10.1088/1742-6596/2167/1/012021>

9. W.C. Fang, X.X. Huang, J.H. Tan et al., Proton linac-based therapy facility for ultra-high dose rate (FLASH) treatment. *Nucl. Sci. Tech.* **32**, 4 (2021). <https://doi.org/10.1007/s41365-021-00872-4>
10. E. Oponowicz, H. Owen, Superconducting Gantry Design for Proton Tomography, in proceedings of IPAC2017, Copenhagen, Denmark, pp 4795–4797 (2017). <https://doi.org/10.18429/JACOW-IPAC2017-THPVA140>
11. Y.Q. Yang, W.C. Fang, X.X. Huang et al., Static superconducting gantry-based proton CT combined with X-ray CT as prior image for FLASH proton therapy. *Nucl. Sci. Tech.* **34**, 11 (2023). <https://doi.org/10.1007/s41365-022-01163-2>
12. Y. Zhang, W.C. Fang, X.X. Huang et al., Design, fabrication, and cold test of an S-band high-gradient accelerating structure for compact proton therapy facility. *Nucl. Sci. Tech.* **32**, 38 (2021). <https://doi.org/10.1007/s41365-021-00869-z>
13. Y. Zhang, W.C. Fang, X.X. Huang et al., Radio frequency conditioning of an S-band accelerating structure prototype for compact proton therapy facility. *Nucl. Sci. Tech.* **32**, 64 (2021). <https://doi.org/10.1007/s41365-021-00891-1>
14. C.E. Ordoñez, N. Karonis, K. Duffin et al., A real-time image reconstruction system for particle treatment planning using proton computed tomography (pCT). *Phys. Procedia.* **90**, 193–199 (2017). <https://doi.org/10.1016/j.phpro.2017.09.058>
15. B. Schaffner, E. Pedroni, The precision of proton range calculations in proton radiotherapy treatment planning: experimental verification of the relation between CT-HU and proton stopping power. *Phys. Med. Biol.* **43**(6), 1579–1592 (1998). <https://doi.org/10.1088/0031-9155/43/6/016>
16. V.A. Bashkurov, R.W. Schulte, R.F. Hurley et al., Novel scintillation detector design and performance for proton radiography and computed tomography. *Phys. Procedia.* **43**(2), 664–674 (2016). <https://doi.org/10.1118/1.4939255>
17. G. Coutrakon, V. Bashkurov, F. Hurley et al., Design and construction of the 1st proton CT scanner, American Institute of Physics American Institute of Physics **1525**, 1 (2013). <https://doi.org/10.1118/1.4939255>
18. A. Kamal, Passage of charged particles through matter, in *Nuclear Physics*. (Graduate Texts in Physics, Springer, Berlin, 2014), pp.1–81. https://doi.org/10.1007/978-3-642-38655-8_1
19. C. Wang, J.H. Tan, X.X. Huang et al., Design optimization and cold RF test of a 2.6-cell cryogenic RF gun. *Nucl. Sci. Tech.* **32**(9), 97 (2021). <https://doi.org/10.1007/s41365-021-00925-8>
20. J.H. Tan, Q. Gu, W.C. Fang et al., Two-mode polarized traveling wave deflecting structure. *Nucl. Sci. Tech.* **26**(4), 040102 (2015). <https://doi.org/10.13538/j.1001-8042/nst.26.040102>
21. C.C. Xiao, J.Q. Zhang, J.H. Tan et al., Design and preliminary test of the LLRF in C band high-gradient test facility for SXFEL. *Nucl. Sci. Tech.* **31**(10), 100 (2020). <https://doi.org/10.1007/s41365-020-00806-6>
22. V. Giacometti, V.A. Bashkurov, P. Piersimoni et al., Software platform for simulation of a prototype proton CT scanner. *Med. Phys.* **44**(3), 1002–1016 (2017). <https://doi.org/10.1002/mp.12107>
23. T. Li, Z.G. Liang, J.V. Singanallur et al., Reconstruction for proton computed tomography by tracing proton trajectories: a Monte Carlo study. *Med. Phys.* **33**(3), 699–706 (2006). <https://doi.org/10.1118/1.2171507>
24. G.H. Chen, J. Tang, S. Leng, Prior image constrained compressed sensing (PICCS): a method to accurately reconstruct dynamic CT images from highly undersampled projection data sets. *Med. Phys.* **35**(2), 660–663 (2008). <https://doi.org/10.1118/1.2836423>
25. S.N. Penfolda, R.W. Schulte, Y. Censor et al., Total variation superiorization schemes in proton computed tomography image reconstruction. *Med. Phys.* **37**(11), 5887–5895 (2010). <https://doi.org/10.1118/1.3504603>
26. R.C. Gonzalez, R.E. Woods, B.R. Masters, Digital image processing, Third Edition. *J. Biomed. Opt.* **14**(2), 029901 (2009). <https://doi.org/10.1117/1.3115362>
27. W. Yu, L. Zeng, A novel weighted total difference based image reconstruction algorithm for few-view computed tomography. *PLoS ONE* **9**(10), e109345 (2014). <https://doi.org/10.1371/journal.pone.0109345>
28. S. Agostinelli, J. Allison, K. Amako et al., GEANT4—A simulation toolkit. *Nucl. Instrum. Methods Phys. Res. Sect. A* **506**(3), 250–303 (2003). [https://doi.org/10.1016/S0168-9002\(03\)01368-8](https://doi.org/10.1016/S0168-9002(03)01368-8)
29. R.F. Hurley, R.W. Schulte, V.A. Bashkurov et al., Water-equivalent path length calibration of a prototype proton CT scanner. *Med. Phys.* **39**(5), 2438–2446 (2012). <https://doi.org/10.1118/1.3700173>
30. R.W. Schulte, S.N. Penfold, J.T. Tafas et al., A maximum likelihood proton path formalism for application in proton computed tomography. *Med. Phys.* **35**(11), 4849–4856 (2008). <https://doi.org/10.1118/1.2986139>
31. D. Williams, The most likely path of an energetic charged particle through a uniform medium. *Phys. Med. Biol.* **49**(13), 2899–2911 (2004). <https://doi.org/10.1088/0031-9155/49/13/010>
32. H. Zhang, G.J. Gang, H. Dang et al., Regularization analysis and design for prior-image-based X-ray CT reconstruction. *IEEE T. Med. Imaging* **37**(12), 2675–2686 (2018). <https://doi.org/10.1109/TMI.2018.2847250>
33. H. Zhang, D. Capaldi, D. Zeng et al., Prior-image-based CT reconstruction using attenuation-mismatched priors. *Phys. Med. Biol.* **66**(6), 064007 (2021). <https://doi.org/10.1088/1361-6560/abe760>
34. D.F. DeJongh, E.A. DeJongh, V. Rykalin et al., A comparison of proton stopping power measured with proton CT and x-ray CT in fresh postmortem porcine structures. *Med. Phys.* **48**(12), 7998–8009 (2021). <https://doi.org/10.1002/mp.15334>

Springer Nature or its licensor (e.g. a society or other partner) holds exclusive rights to this article under a publishing agreement with the author(s) or other rightsholder(s); author self-archiving of the accepted manuscript version of this article is solely governed by the terms of such publishing agreement and applicable law.